Engineering and Technology Journal
Journal homepage: https://etj.uotechnology.edu.iq

Modeling and analysis of thermoelectric atmospheric water generation in the economic city of Iraq

Ammar M. al-Tajer[a*], **Wissam H. Alawee**[b], **Hayder A. Dhahad**[c], **Zakaria M. Omara**[d]

[a] Petroleum Engineering Dept., College of Engineering, University of Kerbala, Karbala, 56001, Iraq.
[b] Control and Systems Engineering Dept., University of Technology-Iraq, Alsina'a street, 10066 Baghdad, Iraq.
[c] Mechanical Engineering Dept., University of Technology-Iraq, Alsina'a street, 10066 Baghdad, Iraq.
[d] Mechanical Engineering Dept, Faculty of Engineering, Kafrelsheikh University, Kafrelsheikh, Egypt.
*Corresponding author Email: me.21.16@grad.uotechnology.edu.iq

HIGHLIGHTS

- Environmental conditions in Qurna, Basra, were analyzed for atmospheric water generation
- Fluent 22 software was used to simulate feasible temperatures for condensation
- Two airflow patterns were tested for effectiveness in temperature and pressure reduction
- Changing airflow patterns altered condensation surface temperatures by up to 38%

ARTICLE INFO

Handling editor: Jalal M. Jalil

Keywords:
Atmospheric Water Generation
Atmospheric Water Harvesting Technologies
Thermoelectric Fresh Water Generator
Thermoelectric
Dew point

ABSTRACT

Atmospheric Water Generation assumes substantial significance as an innovative remedy for addressing water scarcity and augmenting water resilience. This technology facilitates water extraction directly from the atmosphere, presenting a sustainable and decentralized approach to water supply. The investigation into the feasibility of attaining the dew point temperature for a heatsink operating in the climatic conditions of Basra was conducted using Fluent 22.1 software. The minimum dew point temperature under extreme conditions was determined to be 10.52℃. A thermoelectric device was a primary component in cooling the moisture-laden air to produce water from atmospheric air. Simulations were executed using two complementary and two integrated heatsinks under turbulent airflow conditions ranging from 4 to 20 m/s. The results indicated an inverse relationship between heat distribution within the heatsink and fluid flow velocity, emphasizing the crucial role of airflow passage arrangement in the condensation process. Enhancing the heatsink's surface area and reducing airflow quantity proved effective in achieving the dew point temperature. The lowest temperature attained was 9.2℃, featuring intersecting heat exchangers with a flow velocity of 4 m/s. The result indicated that altering the flow pattern affects the condensation process's surface temperature by as much as 38%, while the rise in pressure difference can reach 20%. Under the same operational conditions, the difference in thermal conductivity between two distinct heat exchanger configurations, attributed to pressure variations, is notably 8%. The study concludes that the Qurna region benefits from favorable weather conditions, encompassing temperature and relative humidity, thereby enabling water generation from atmospheric air, notwithstanding the consideration of the dew point temperature as a limiting factor.

1. Introduction

Providing access to clean and potable water is a fundamental requisite for human well-being and economic development. However, numerous regions across the globe encounter substantial impediments in satisfying this imperative demand [1]. The Basra region in southern Iraq is no exception to this global water crisis [2].

Amidst its arid climatic conditions, accelerated urbanization, and escalating water requirements, Basra confronts pronounced challenges related to water scarcity. Within this framework, it is imperative to develop and implement innovative and sustainable technologies expeditiously to effectively mitigate the prevailing water crisis in the region [3].

To address water scarcity, researchers [4-9] have investigated a range of Atmospheric Water Generation AWG techniques, including thermoelectric systems, active refrigeration, desiccant adsorption, passive cooling, fog and dew harvesting, and solar-powered sorption-based technologies, across various regions, notably India and Egypt. These studies aimed to enhance the efficiency of AWG systems through advancements in materials and design and by integrating AWG with clean energy solutions such as CO_2 capture and photocatalytic water splitting for fuel production. Solar-driven air-water harvesting

http://doi.org/10.30684/etj.2024.145961.1671
Received 15 January 2024; Received in revised form 25 March 2024; Accepted 02 April 2024; Available online 29 April 2024
2412-0758/University of Technology-Iraq, Baghdad, Iraq

technology was also explored, identifying key challenges and proposing innovative device designs. Experiments conducted in India employed composite materials, while in Egypt, desiccant solutions were used to successfully generate water from atmospheric air, showcasing the viability of these approaches in combating water scarcity.

In a related context, Joshi et al. [10] explored using thermoelectric mechanisms for atmospheric water generation. Joshi et al. [10] conducted a research endeavor on experimentally evaluating a Thermoelectric Fresh Water Generator (TFWG) predicated on the Thermoelectric Cooling Effect. The primary objective of this generator is the extraction of moisture from the ambient humid air, rendering it especially advantageous for inhabitants in coastal and humid regions characterized by a relative humidity surpassing 60% and a concurrent shortage of potable water. Experimental results indicate that incorporating an internal heatsink yields an 81% augmentation in the quantity of water generated over 10 hours compared to scenarios where the internal heatsink is not deployed. Eslami et al. [11] offer a thorough thermodynamic analysis of a system employing thermoelectric coolers TECs for water production from humid air. This system integrates multiple TECs, an air circulation fan, dual cold and hot air conduits, heat sinks, and solar cells to supply power to the TECs and the fan. The outcomes demonstrate the system's capability to yield 26 ml of water within a single hour, sourced from air possessing a relative humidity of 75% and a temperature of 318 K while consuming a mere 20W of electrical power. Chaves et al.[12] studied water extraction from the atmosphere through condensation, employing a specialized duct with fins and thermoelectric coolers, as simulated using ANSYS FLUENT software. The investigation unveiled that the devised apparatus can yield a maximum of 44 milliliters of water per hour in locales characterized by elevated humidity, such as Mumbai. Esfe et al. [13] explore the influence of incorporating a thermoelectric system TEC within an air-water generator. The experimental setup comprises 12 samples, each featuring cold surface temperatures from 1 ℃ to 12 ℃. These experiments were conducted under consistent ambient conditions of 35 ℃ and 80% relative humidity. The investigation entails visualizing properties such as velocity and temperature fields, velocity contours, isotherms, and mass fraction gradients. The maximal production rate was observed at a minimal cold surface temperature, yielding 0.323 $kg.m^{-2}.hr^{-1}$.

This research, conducted under the suitable environmental conditions of the Qurna region in southern Iraq, aims to numerically analyze a heat sink designed for heat absorption in atmospheric water generation. This research endeavors to perform numerical analysis on a heatsink engineered for heat absorption for atmospheric water generation. Utilizing Fluent 2022 R1 software, the investigation will delineate the temperature distribution and pressure profiles corresponding to two distinct operational modes of the heatsink. The study aims to measure heat sinks' energy consumption and temperature distribution in a specific arrangement to understand the limits of turbulent air velocity for condensation. These findings are integral to evaluating the feasibility of implementing a condensation process within the specified geographical area.

Based on data that indicates the shortage of potable water due to sources of pollution occurring in southern Iraq [14,15], In response to the scarcity of potable water and the presence of contaminants in existing water sources, the investigation explores the prospect of generating water from atmospheric moisture. Preliminary data on the temperature distribution throughout Iraq, specifically in the Qurna district, as shown in Figure1 (A and B), along with the relative humidity in Figure 1 (C and D), highlight the distinctive climatic conditions for establishing such systems.

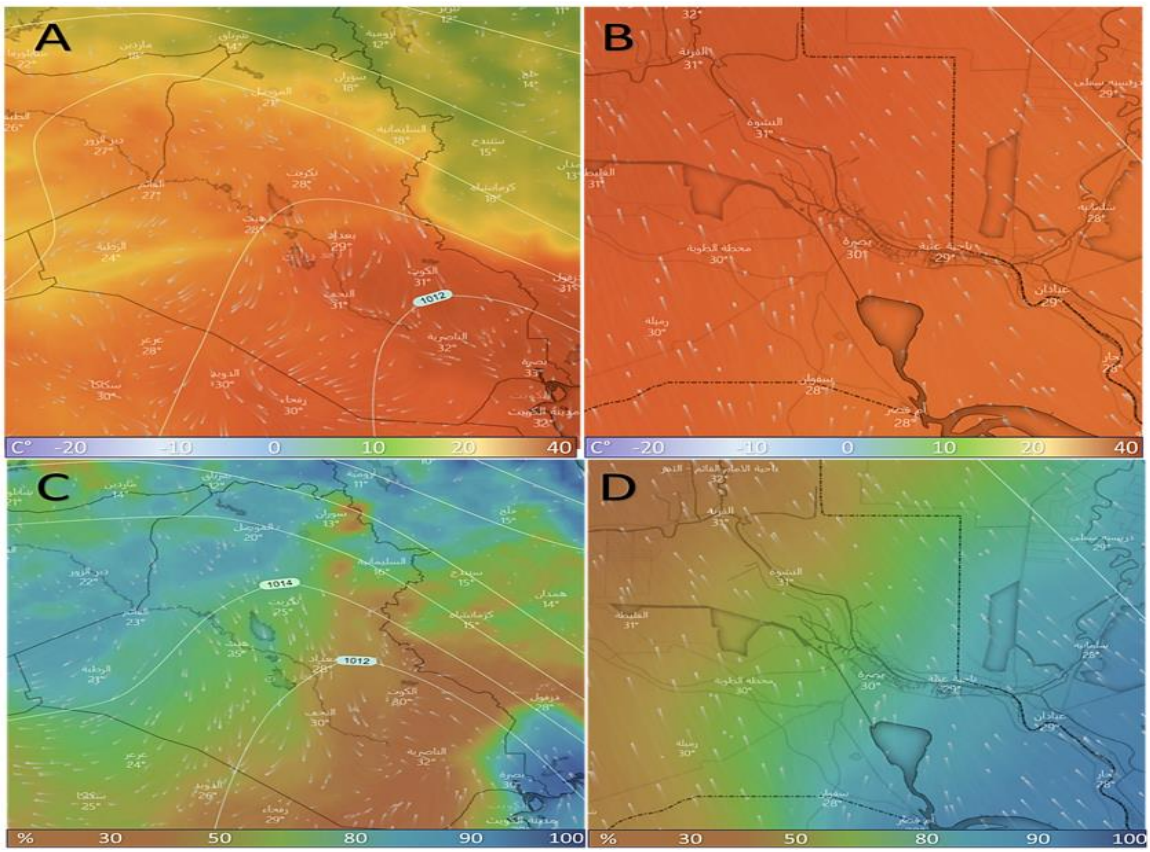

Figure 1: Maps for Temperature distribution in A) ambient temperature in Iraq. B) ambient temperature in Basra, Qurna 2: C) Relative humidity in Iraq. D) Relative humidity in Basra, Qurna

2. Methodology

Diverse methodologies exist to facilitate water generation from atmospheric air, with one involving cooling metallic bodies to temperatures below the dew point. This process leverages the abundance of solar energy harnessed to power a thermoelectric device responsible for cooling the heatsink. The initial phase involves a meticulous study of environmental conditions to inform the arrangement of the water generation device. The data was obtained and analyzed at the Qurna station in southern Iraq, at longitude N:47.45° and latitude E: 30.94°. This location is part of the Ministry of Agriculture's Meteorological Center, situated in the northern area of the Basra Governorate, a region notable for the confluence of the Tigris and Euphrates rivers, as shown in Figure 2 (A and B). An initial environmental study spanned eighteen months to gather necessary climatic data crucial for the setup and optimization of the water generation device. The core of the water generation system is a TEC1-12715 thermoelectric cooling (TEC) device powered by solar energy. This setup leverages the abundant solar radiation in the region to operate the TEC device, which facilitates water condensation from the air by cooling a metallic heatsink below the dew point temperature. In order to achieve the best condensation process, heat sinks were used to increase the surface area for air contact with the cooling surface, as will be explained in the geometry section later on. A specific correlation was utilized for calculations to determine the dew point temperature for given conditions of dry bulb temperature and relative humidity in the Qurna district, as detailed in reference [16].

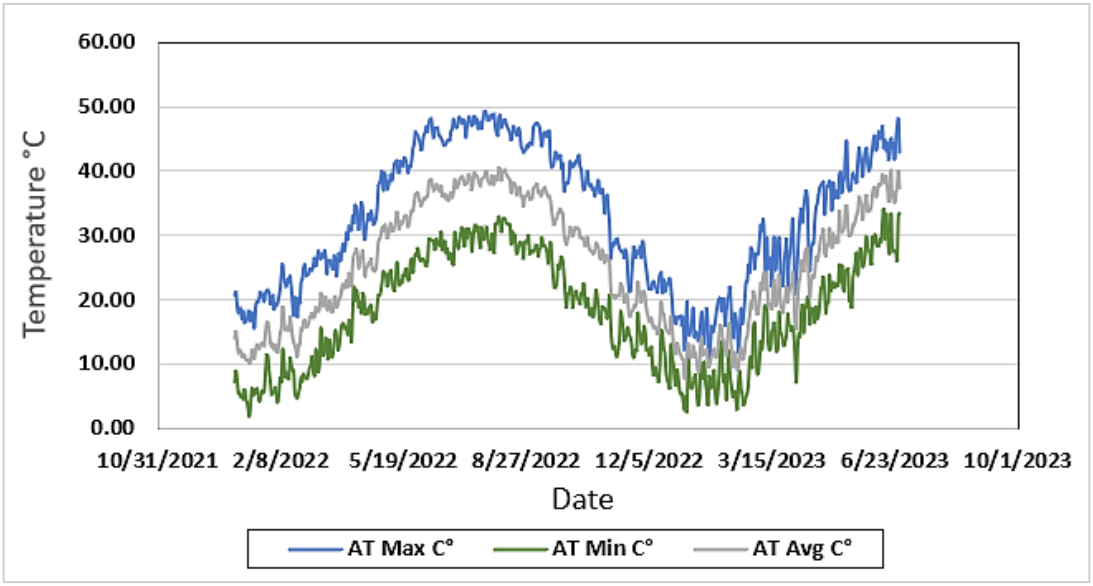

(A)

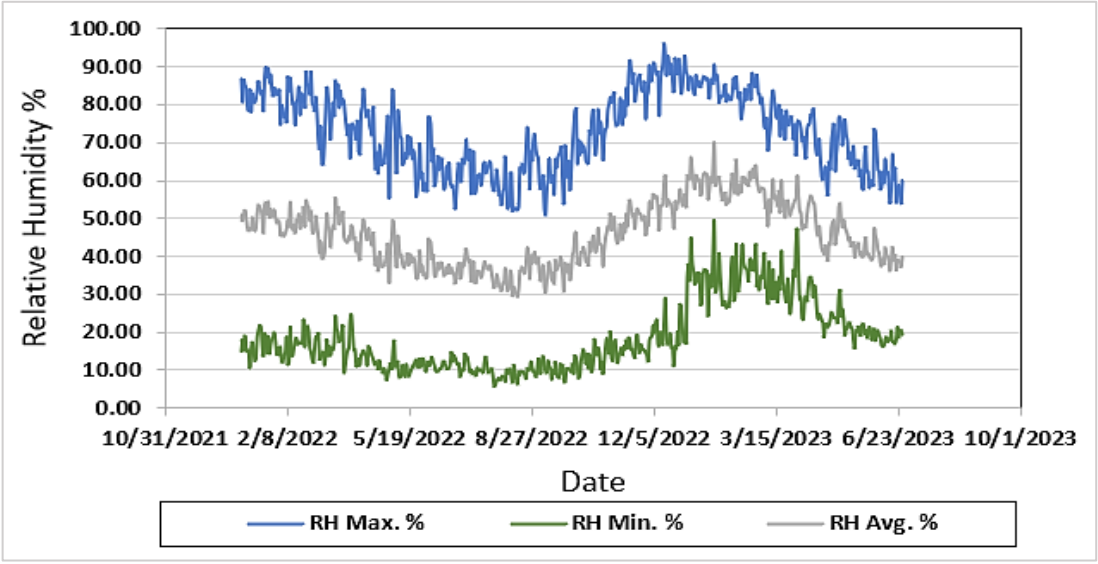

(B)

Figure 2: Data in Al-Qurna throughout the year A) Temperature, B) The relative

$$TD = T - (\frac{100-RH}{5}) \quad (1)$$

On July 1, as illustrated in Table 1, dew point temperatures ranged from 10.52°C to 39.9°C, marking the lowest and highest recorded values, respectively.

Environmental data, including temperature and humidity ranges, were collected in early July, as indicated in Table 2 [17,18].

Table 1: Dew point temperature in summer season

No.	Date	Min Dew Point C	Max. Dew Point C	Avra. Dew Point C
1	1/5/2022	4.56	35.15	19.85
2	1/6/2022	7.9	35.95	21.92
3	1/7/2022	10.52	39.91	25.32
4	1/8/2022	13.09	38.13	25.61
5	1/9/2022	9.97	39.86	25.25
6	1/10/2022	4.66	37.01	20.41

Table 2: Humid air properties

Date	Case	Temperature ℃	Relative humidity %	Density	Date	Case	Temperature ℃
1/7/2022	Min.	28.46	10.32	1.2490	0.02566	1003.47	1.826×10^{-5}
	Max.	46.79	65.64	1.1768	0.02826	1003.32	2.009×10^{-5}

This data underpins the operational threshold for the thermoelectric device, dictating the necessity to cool the heatsink below these dew point temperatures to induce water condensation.

The TEC device's operation aimed to achieve the lowest possible temperature conducive to water condensation without reaching the freezing point [19]. The target was to maintain the cooling effect at a minimum of one degree Celsius above freezing, utilizing the electrical energy generated by a solar photovoltaic (PV) panel.

2.1 Geometry

Figure 3 illustrates an aluminum heatsink with dimensions detailed in the accompanying figure. The rear end features an attachment point for the thermoelectric device, facilitating heat dissipation Figure 4 (A and B). The specific thermoelectric type and its associated properties are presented in Table 3.

Table 3: Humid air properties

Property	Value	Unit
Seebeck coefficient	210	μV/K
Electrical conductivity	1.1	S/m
Thermal conductivity	1.5	W/m•K
Maximum cooling power	136	W
Maximum temperature difference	70	K
Maximum input voltage	15.4	V
Maximum input current	15	A
Dimensions	40 mm × 40 mm × 3.75 mm	-
Weight	50	g

The system comprises a heatsink connected at the rear to a thermoelectric device, facilitating heat removal and powered by solar energy. The rear surface of the heatsink is maintained at a constant temperature of 1 degree Celsius. Air, representative of the specific humidity and temperature conditions simulating the Al-Qurna region, flows through the heatsink opening, undergoing cooling by the cold surface. The airflow exhibits a turbulent pattern, with 4, 5, 10, and 20 m/s velocities.

Two configurations are implemented to establish airflow paths and determine the heat distribution. In both configurations, identical heatsinks are utilized, featuring equivalent metal configurations albeit arranged differently, as delineated in Figure 5. The first configuration, referred to as "Case A," employs two opposing heatsinks, complementarily forming a single longitudinal air passage as shown in Figure 5A. The second configuration, referred to as "Case B," involves the merging or interlocking of fins from each exchanger to create narrow condensation passages, shown in Figure 5B. By maintaining uniform material costs and a consistent energy supply for airflow (at velocities of 4, 5, 10, and 20 m/s) through the heatsink passages, the objective is to ascertain optimal performance in terms of temperature and pressure distributions.

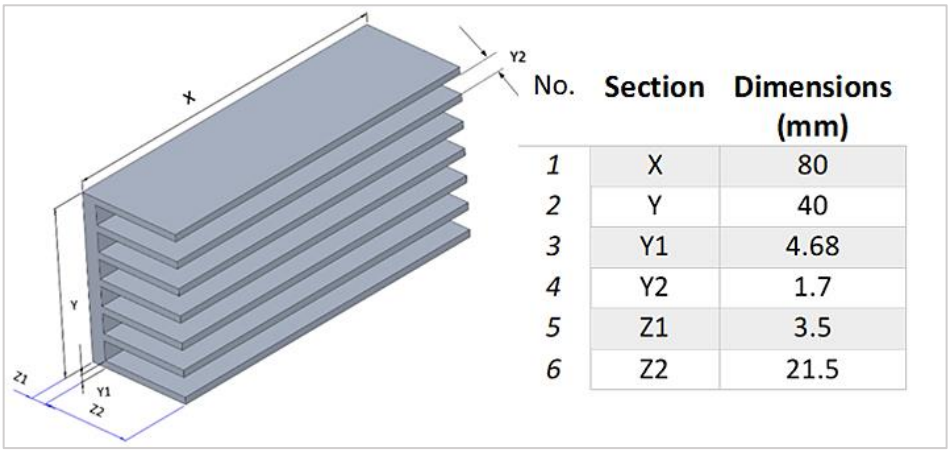

No.	Section	Dimensions (mm)
1	X	80
2	Y	40
3	Y1	4.68
4	Y2	1.7
5	Z1	3.5
6	Z2	21.5

Figure 3: Aluminum heat sinks

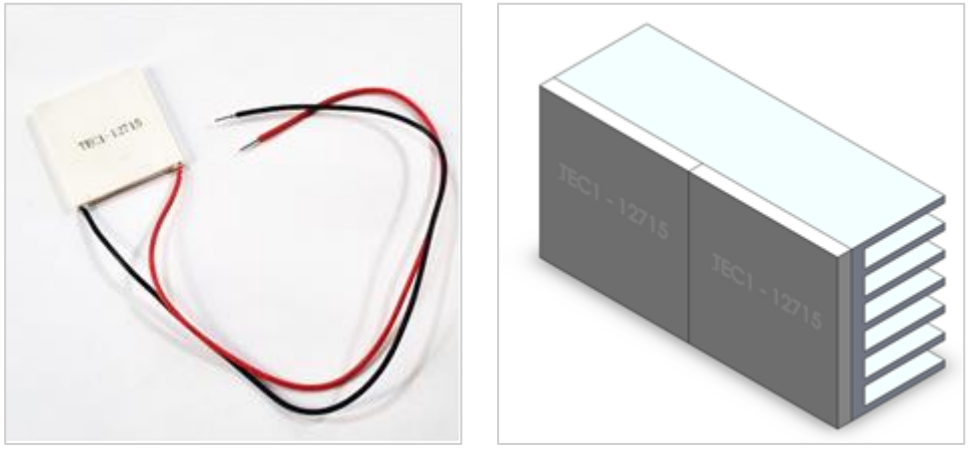

(A) **(B)**

Figure 4: Thermoelectric of A) thermoelectric type, B) fix on heat dissipation

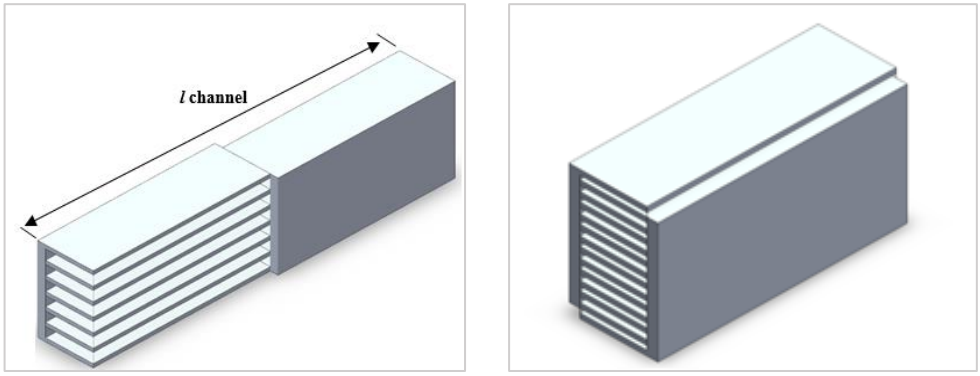

(A) **(B)**

Figure 5: Geometry of two flow patterns A) Case 1, B) Case 2

2.2 Governing equations

According to the first law of thermodynamics, the power consumption of the thermoelectric is

$$\mathrm{PTEC} = \mathrm{Qh} - \mathrm{Qc} \tag{2}$$

Utilizing an energy balance analysis on a thermoelectric cooler allows for the computation of both the cooling power and the heat dissipation from the hot side of the thermoelectric cooler [20-22].

$$Q_c = S_m I\, T_c - \frac{I^2 R_m}{2} - K_m \Delta T \tag{3}$$

$$Q_h = S_m I\ T_h - \frac{I^2 R_m}{2} - K_m \Delta T \quad (4)$$

where

$$\Delta T = T_h - T_c \quad (5)$$

Modeling thermoelectric coolers requires the definition of specific parameters, which include I_{max}, V_{max}, ΔT_{max}, and Q_{max}, in addition to the hot and cold sides temperature (T_h) and (T_c) of a TEC, respectively. These four fundamental characteristics uniquely identify each thermoelectric cooler.

$$R_m = \frac{(T_h - \Delta T_{max}) V_{max}}{T_h I_{max}} \quad (6)$$

$$S_m = \frac{V_{max}}{T_h} \quad (7)$$

$$K_m = \frac{(T_h - \Delta T_{max}) V_{max} I_{max}}{2 T_h I_{max}} \quad (8)$$

Rm signifies electrical resistance, Sm represents the Seebeck coefficient, and Km represents thermal conductivity. So, the Equation 2 will be.

$$\mathrm{PTEC} = \mathrm{Sm\ I\ \Delta T} + \mathrm{I^2\ R_m} \quad (9)$$

COP, or Coefficient of Performance, is a measure used to evaluate the efficiency of a thermoelectric system or device [20].

$$COP = \frac{Q_c}{P_{TEC}} \quad (10)$$

Air will lose heat according to the following Equation [21] when it passes through the cooling channel.

$$Q_c = \dot{m}_c (h_{air-in-c} - h_{air-out-c}) \quad (11)$$

$$Q_C = \dot{m}_c C_{p-c} (T_{air-in-c} - T_{air-out-c}) \quad (12)$$

Cp represents air heat within the cold channel, and h refers to the enthalpy of humid air in joules per kilogram. It's worth noting that the enthalpy depends on the specific humidity (ω) [20].

$$h = Cp(T - 237) + \omega(250.3 + 1.86(T - 273)) * 1000 \quad (13)$$

Heat transfer within the channels can also be correlated with the temperature difference between the airflow and the hot and cold surfaces using the LMTD (Log Mean Temperature Difference) method [21].

$$Qc = \frac{\Delta T_{LMTD-coldside}}{R_c} \quad (14)$$

So, the Equation (14) will be [22].

$$\Delta T_{LMTD-coldside} = \frac{[(T_{air-in-c} - T_c) - (T_a - T_c)]}{in\ (\frac{T_{air-in-c} - T_c}{T_a - T_c})} \quad (15)$$

The contact resistance between thermoelectric coolers and the heatsink connected to the cold channel is so minimal that it can be disregarded, as shown in Equation (16) [11].

$$R_{equ} = \frac{R'_{t,c}}{N_{TEC} l_{TEC} w_{TEC}} \quad (16)$$

The N_{TEC} is the number of thermoelectrics, and l_{TEC} and w_{TEC} represent the length and width of thermoelectrics, respectively. The resistance of base heat sinks is given by :

$$R_{equ} = \frac{z_1}{k_s l_{channel} w_{conv}} \tag{17}$$

where Z_1, $l_{channel}$ is the length of the channel, and $w_{channel}$ is the width of the channel in Figures 3 and 5 and k_s is the thermal conductivity of base plate material [23].

$$R_{equ} = \frac{1}{\eta_0 A_t h_{conv}} \tag{18}$$

where the η_0 is given by

$$\eta_0 = 1 - \frac{N_{fin} A_f}{A_t}(1 - \eta_f) \tag{19}$$

The A_f represents the area of the fin, which is given by

$$A_f = 2 w_{fin} l_c \tag{20}$$

The Characteristic length will be calculated by

$$l_c = l_{fin} + \frac{t_{fin}}{2} \tag{21}$$

To elucidate the connection between thermoelectric and the heat sink, a section of the heat sink attached to the thermoelectric material was illustrated as shown in Figure 6A. Furthermore, to demonstrate the heat transfer process resulting from the heat extraction by the heat sink, a portion of the fins was selected to detail the stages of heat transfer from the air to the thermoelectric material as indicated in Figure 6B. The stages of the heat transfer process from the air to the heat sink consist of a series of resistances, as depicted in Figure 6C.

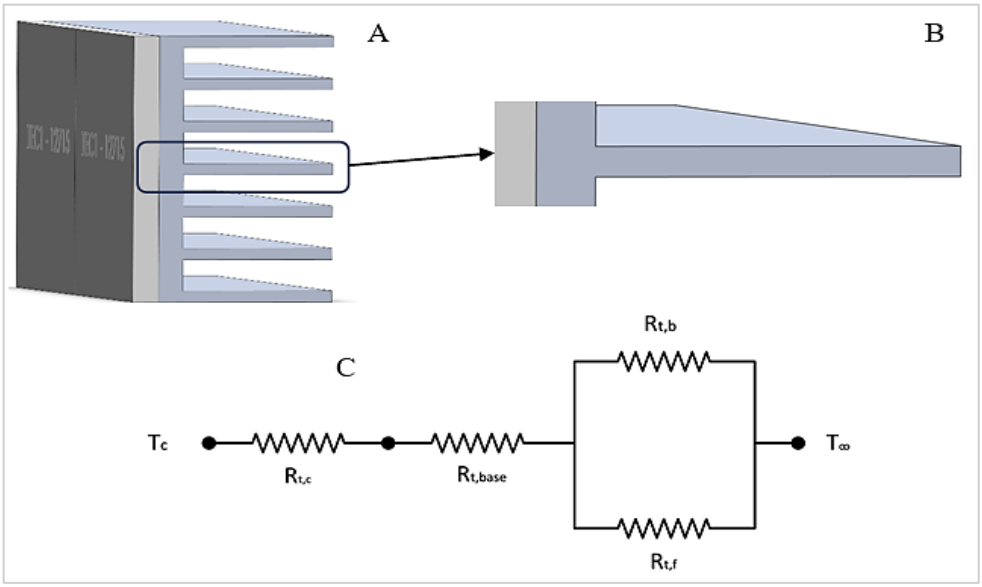

Figure 6: A) heat sink B) singular fin C) Thermal resistances of the cold side of thermoelectric with heatsink in the channel

At represents total area [11]

$$A_t = l_{hole} l_{channel} N_{hole} + (2N_{hole} - 2) H_{hole} l_{chanel} \tag{22}$$

The fin efficiency η_0 is calculated by [11]

$$\eta_0 = \frac{tanhml_c}{ml_c} \tag{23}$$

where M, p, Ac “cross-section area” are:

$$m = \sqrt{\frac{h_{conv}p}{k_s A_s}} \quad , p = 2\left(w_{fin} + t_{fin}\right), Ac = w_{fin}t_{fin}$$

Convection heat transfer coefficient hconv. is calculated by [21].

$$h_{conv} = \frac{Nuk_f}{D_{hyd}} \tag{24}$$

where kf is the thermal conductivity of air. The Nusselt number is calculated by [21] for cooling flowing air.

$$Nu = 0.023Re^{0.8}Pr^{0.3} \tag{25}$$

where the Reynolds number Re of air following is [24].

$$Re = \frac{u_{average}\, D_{hyd}}{v} \tag{26}$$

For the hydraulic rectangle channel calculated by [22].

$$D_{hyd} = \frac{4A_{hole}}{P_{hole}} = \frac{4\, l_{hole}H_{hole}}{(2\, l_{hole}+H_{hole})} \tag{27}$$

So, the total resistance on the cold side is calculated by:

$$Rc = R_{t,base} + R_{equ} \tag{28}$$

2.3 Modeling and simulation

A mathematical model was formulated to analyze airflow under a defined set of conditions, with a relative humidity of 37% and a temperature of 28 ℃. The model aimed to ascertain the thermal distribution in heat sinks based on the adopted theoretical framework. The modeling procedure was executed using ANSYS Fluent software, version 22 R1.

2.3.1 Governing equations

For transient state airflow inside the heatsink with turbulent flow, enhanced Near-Wall Treatment is considered [25].

2.3.1.1 Continuity equation

The principle asserts that the mass of a fluid within a defined spatial domain remains constant over time in the absence of mass sources or sinks. This concept can be formalized mathematically through the following Equation:

$$\frac{\partial p}{\partial z} + \nabla \cdot (\rho v) = 0 \tag{29}$$

2.3.1.2 Momentum equation

The momentum equation, a fundamental tenet in fluid dynamics, elucidates the transient characteristics of airflow or any fluid flow. Recognized as the Navier-Stokes equation, it delineates the motion of fluid particles and their interaction with external forces. The generalized formulation of the transient momentum equation for compressible flows, such as air, is articulated as follows:

$$\rho\left(\frac{\partial v}{\partial t} + v.\nabla v\right) = -\nabla p + \mu\nabla^2 v + \rho g \tag{30}$$

2.3.1.3 Energy equation

The energy equation articulates the conservation of energy principles in transient airflow. It posits that the temporal variation of energy within a specified control volume equals the net energy flux across the control volume's surface, encompassing contributions from convection, conduction, and heat sources.

$$\frac{\partial \rho e}{\partial t} + \nabla \cdot (\rho e v) = \nabla \cdot (k \nabla T) + Sh \tag{31}$$

2.3.1.4 Standard k-ε

Turbulent flow was characterized utilizing the transport equations corresponding to the standard k-ε model. In this model, the variable 'k' denotes the turbulent kinetic energy inherent in the fluid flow. Turbulent kinetic energy is a metric for assessing the energy attributed to turbulent fluctuations within the flow, quantifying the kinetic energy encapsulated within turbulent eddies [26].

$$\frac{\partial}{\partial t}(\rho k) + \frac{\partial}{\partial x_i}(\rho k u_i) = \frac{\partial}{\partial x_j}\left[\left(\mu + \frac{\mu_t}{\sigma_k}\right)\frac{\partial k}{\partial x_j}\right] + G_k + G_b - \rho\varepsilon - y_n + S_k \tag{32}$$

The variable 'ε' within the framework of the k-ε model signifies the rate of dissipation of turbulent kinetic energy. Turbulent flows are distinguished by the persistent energy transfer across various scales of eddies. A portion of this energy undergoes dissipation as heat, primarily influenced by viscosity and turbulence interactions. The transport equation for 'ε' elucidates the pace at which turbulent kinetic energy is transformed into thermal energy (dissipation) under the influence of turbulence [26].

$$\frac{\partial}{\partial t}(\rho \varepsilon) + \frac{\partial}{\partial x_i}(\rho \varepsilon u_i) = \frac{\partial}{\partial x_j}\left[\left(\mu + \frac{\mu_t}{\sigma_\varepsilon}\right)\frac{\partial \varepsilon}{\partial x_j}\right] c_1 \varepsilon \cdot \frac{\varepsilon}{k}(G_k + G_{3\varepsilon} G_b) - C_{2\varepsilon}\rho\frac{\varepsilon^2}{k} + S_\varepsilon \tag{33}$$

Implementing enhanced wall treatment in turbulent flow simulations is pivotal in ensuring the accurate representation of heat transfer phenomena, particularly in scenarios such as cooling applications [27]. Employing specialized modeling techniques, this approach effectively resolves velocity and temperature gradients near the wall, a critical aspect for precise heat transfer characterization.

This methodology presents a judicious compromise, balancing accurate resolution of the near-wall viscous sublayer while concurrently managing computational costs. Consequently, it facilitates precise predictions of flows near walls, encompassing heat transfer dynamics, obviating the need for a comprehensive resolution of the entire boundary layer.

$$y^+ = \frac{u_\tau y}{v} \quad \text{where} \quad u_\tau = \frac{\sqrt{\tau_w}}{\rho} \tag{34}$$

So, to achieve the best results for turbulent flow, the cells near the wall were reduced in size to simulate the laminar sublayer effect, as illustrated in the mesh.

2.3.2 Geometry and Mesh

Before beginning numerical simulations, it is crucial to carefully select the appropriate mesh resolution for the problem at hand. Figure 7 presents the geometric representation of Case 1, in which the cells have a hexahedral configuration. To determine the numerical simulation's robustness to variations in mesh size, Figure 8 illustrates an analysis conducted with six different cell counts. The results are compared, focusing on achieving the lowest internal surface temperature through air exchange. After thoroughly evaluating errors and variations, the optimal mesh size was identified as 1,210,028 cells.

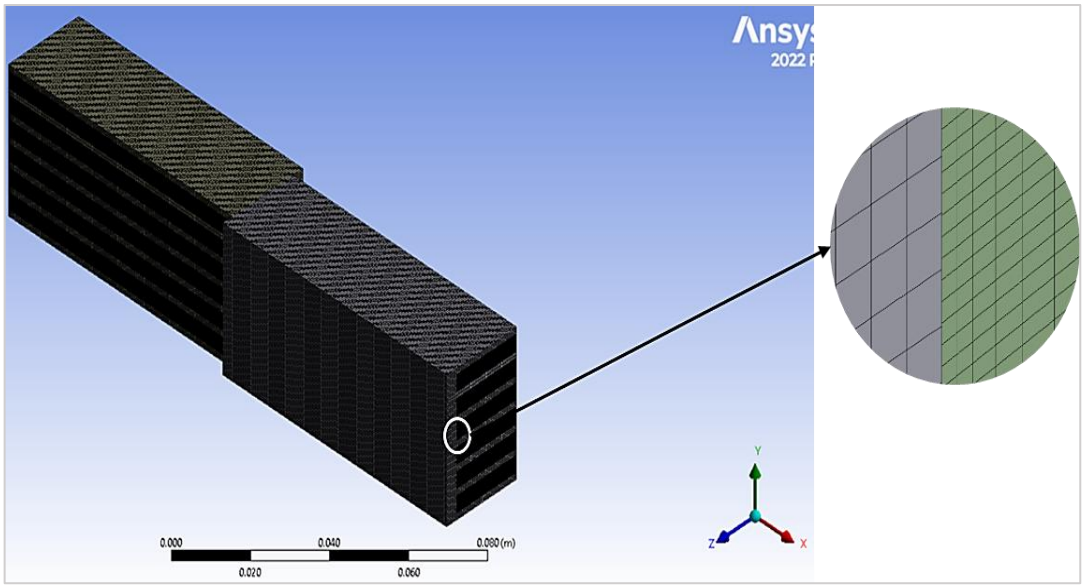

Figure 7: Geometry mesh

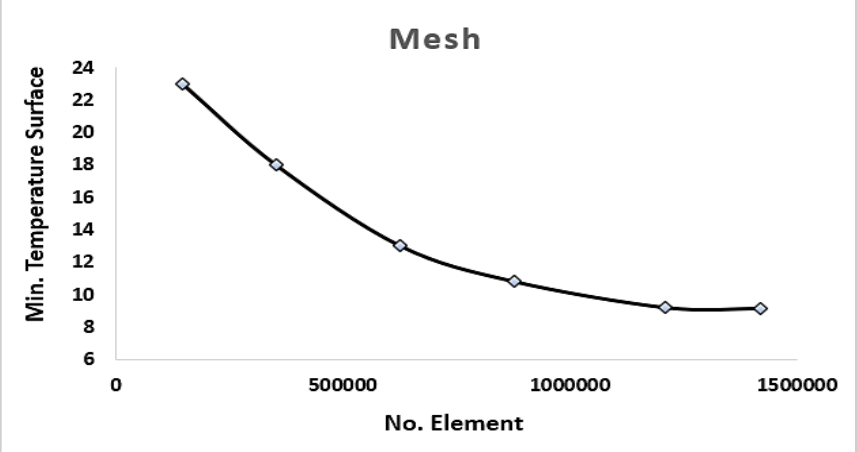

Figure 8: Mesh independent chart

2.3.3 Solution procedure

The subsequent procedural steps are undertaken prior to initializing the calculations in ANSYS Fluent.

2.3.3.1 Material Properties

The properties of the fluid, in this instance air, are defined with specified parameters as outlined in Table 2. For solid materials, aluminum alloy 1050 is used, characterized by the following specific properties at room temperature: a Density (ρ) of 2.7 g/cm³, a Specific Heat Capacity of 0.897 J/g.℃, and a Thermal Conductivity (k) of 200 W/(m.K) [28].

2.3.3.2 Boundary Conditions

Specific boundary conditions relevant to the given problem are defined, incorporating inlet conditions characterized by velocities of 4, 5, 10, and 20 m/s, along with a consistent temperature of 29°C. For the outlet flow, the flow rate weighting is set to 1, and the wall temperatures for cooling walls are maintained at a constant surface temperature of 1°C.

2.3.3.3 Solver Settings

Select the appropriate solver, in this case, a transient solver, and include the effect of gravity in the y-direction, represented by a gravitational acceleration of -9.81 m/s².

2.3.4 Residuals

The graphical representation delineates a graph depicting the residuals corresponding to the continuity, velocity components, pressure, and energy equations during a transient Computational Fluid Dynamics (CFD) simulation. The simulation is configured with a specified number of time steps set at 1000, each with a time step size of 0.0004 seconds. The temporal evolution leading to the achievement of a convergent solution is depicted in Figure 9. As shown in Figure 9, the equations for the conservation of mass and momentum in three directions, in addition to the energy equation and the turbulent flow equation, have been approximately constant in the rate of change after 740 iterations and have not changed. Through Figure 9, it is evident that the derived results are stable.

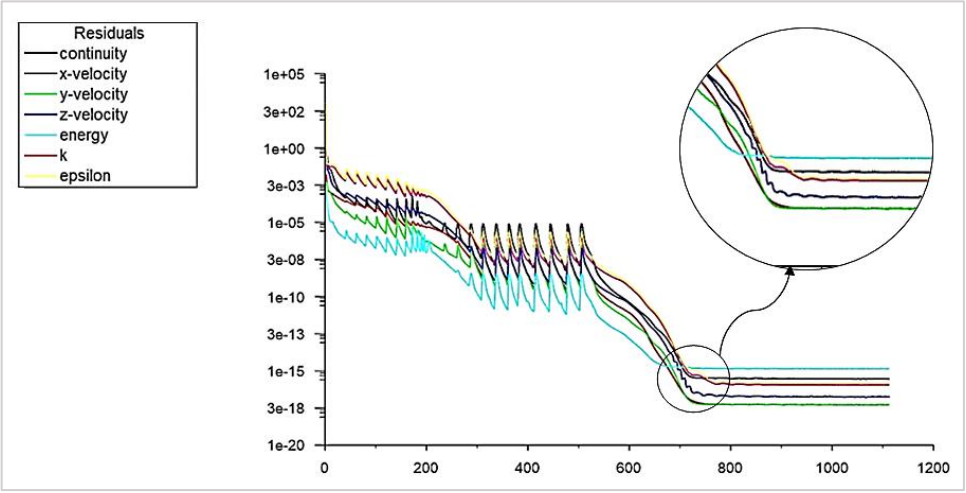

Figure 9: Convergence history for simulation equations

3. Validation

In contrast to the work done by Kanargi et al. [27], which involved both experimental and numerical analyses of airflow over a heatsink, the present study adopts a similar methodology. Kanargi et al. [27] utilized Fluent software to model airflow, comparing the numerical results with experimental observations under specific conditions. This comparison revealed a noticeable alignment between the experimental and numerical data, as illustrated in Figure 10. The findings indicated a significant convergence in the Nusselt number, especially at low Reynolds numbers. One factor contributing to the observed discrepancies is the asymmetry in the Prandtl number between the practical and theoretical approaches, as detailed in Equation 25.

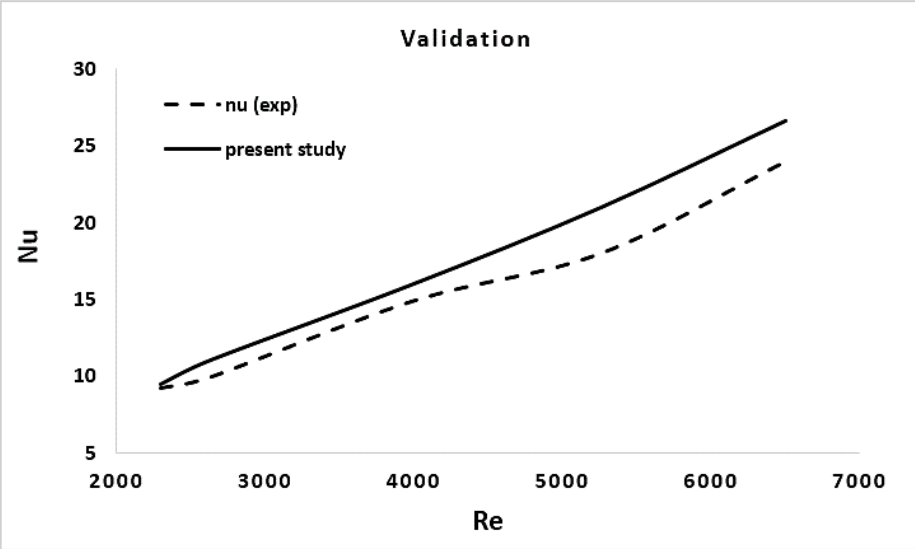

Figure 10: Comparison of numerical Nusselt numbers of present work with experimental [27]

4. Results and discussion

Figure 11 depicts the temperature distribution across the heatsink in Case 1 at various air velocities, specifically 4, 5, 10, and 20 meters per second. It is evident that as velocity increases, the prominence of temperature distribution on the heatsink decreases. This observed distribution highlights the significant influence of the inlet region on heat distribution along the heatsink walls.

The results indicate that at the lowest air flow speed of "4 m/s," the heat exchange is more pronounced, as shown in Figure 11A. Meanwhile, a slight increase in air speed impacts the temperature distribution, as indicated by the temperature gradient near the surface shown in Figure 11B. At higher flow speeds, as depicted in Figures11C and 11D, the effect on temperature becomes difficult to interpret due to the rapid air flow and the unclear process of heat conduction. Moreover, the diagram suggests that the lowest temperature is concentrated at the four corners near the exit edges, resulting from the heat sink operation along the heat exchanger. This pattern leads to heat dissipation along the air passage, signaling the beginning of the condensation process near the walls adjacent to the air outlet. The lower surface temperatures at the end of the heat sink wall are attributed to the reduced air temperature at the end, resulting in a smaller temperature difference.

Combining the two heatsinks to achieve more confined air passages, as illustrated in Figure 12, the modeling process is conducted under the same conditions as in the initial comparative analysis. The subsequent comparison reveals the temperature distribution for the combined heat exchangers and outlines the resulting impact on each.

Figure 12 illustrates the temperature distribution on the surface of the heat sink at various speeds. The surface temperature distribution is clearly visible at the lowest speed 4 m/s, as shown in Figure 12A. When the air speed is increased to 5 m/s, the heat distribution on the surfaces of the heat sink decreases, but the difference is minimal compared to case 12B. As the air speed is further increased to 10 and 20 m/s, it becomes more challenging to discern the temperature distribution on the surfaces of the heat sink, as indicated in Figures 12C and D. As depicted in Figures 13a and b, particularly near the air outlet, this observation is attributed to the sufficient time allowed for heat exchange between the heat sink and the air. The lowest temperature is recorded at the outlet of the integrated heat exchanger, indicating the beginning of the condensation process. At this point, the phase transformation process takes place to form a dew drop due to the surface temperature below the dew drop.

Figure 14 illustrates the thermal distribution for two distinct heatsink cases under an airflow velocity of 5 m/s. The external surface temperatures near the thermoelectric device are maintained at a constant 1°C. The depicted figures reveal differences in thermal distribution between the two cases. In Figure 14A, an increase in heat exchange with the air at the outlet is noticeable, resulting in lower temperatures in the region near the air outlet of the heatsink. In Figure 14B, the surface temperature is significantly reduced due to the cooling process, which encourages the condensation of dewdrops on the internal surfaces, as shown in Figure 14B.

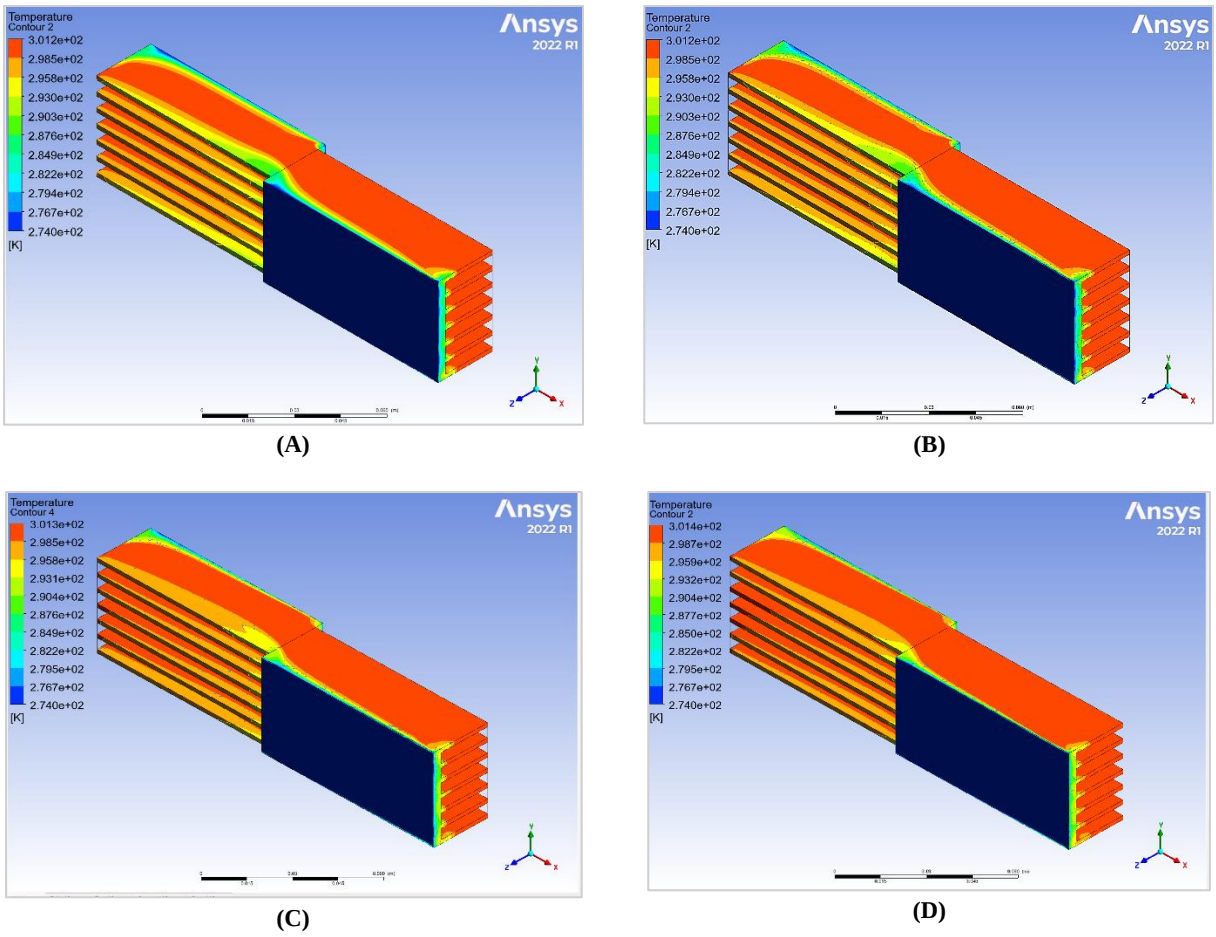

Figure 11: Temperature distribution of heatsink of the first case with A) 4, B) 5, C) 10, and D) 20 m/s

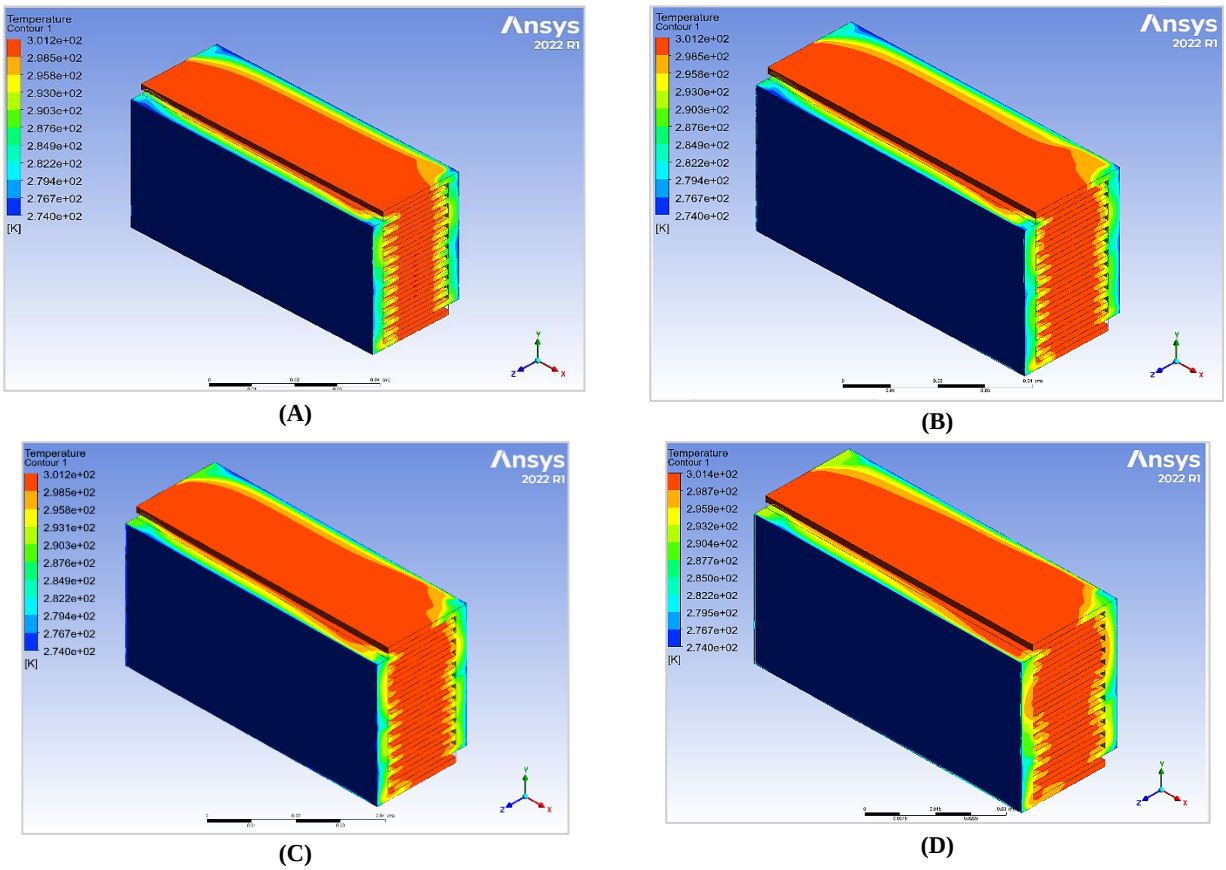

Figure 12: Temperature distribution of heatsink of the second case with A) 4, B) 5, C) 10, and D) 20 m/s

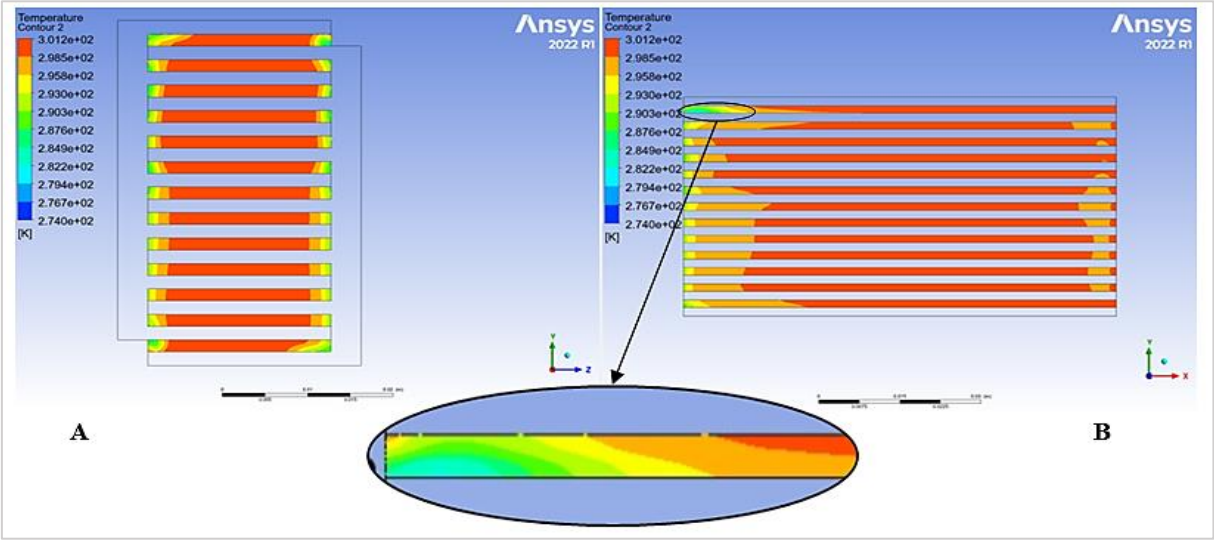

Figure 13: Temperature distribution of air of the second case with A) rear end view (air outlet), B) side view at 4 m/s

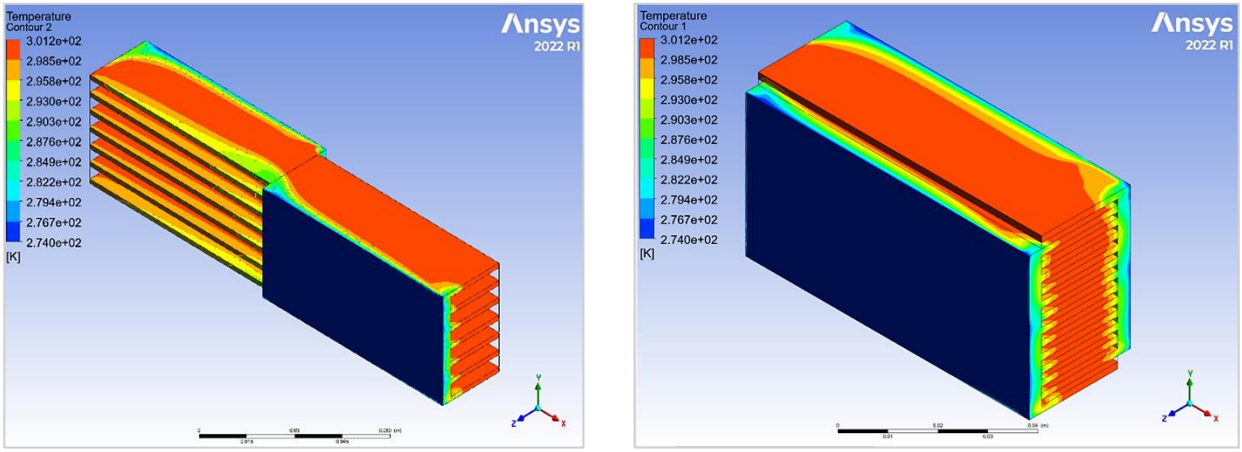

(A) **(B)**

Figure 14: Temperature distribution of heatsink for 2 cases A) case 1 and B) case 2

Figure 15 illustrates the impact of two distinct heatsink configurations on airflow velocity distribution, set at 5 m/s, as the air moves through the channels. This depiction includes the inlet region, the airflow path within the passage, and the effect of the adjacent layer on the airflow velocity at the heatsink walls.

In Figure 15A, the initial condition of airflow is shown, where near the fins, the velocity reaches its minimum value, thereby enhancing the heat exchange process. On the other hand, Figure 15B demonstrates a significant effect where the flow velocity decreases through narrow passages due to fin interference. This phenomenon improves surface heat transfer, leading to a lower dew point temperature than the initial condition.

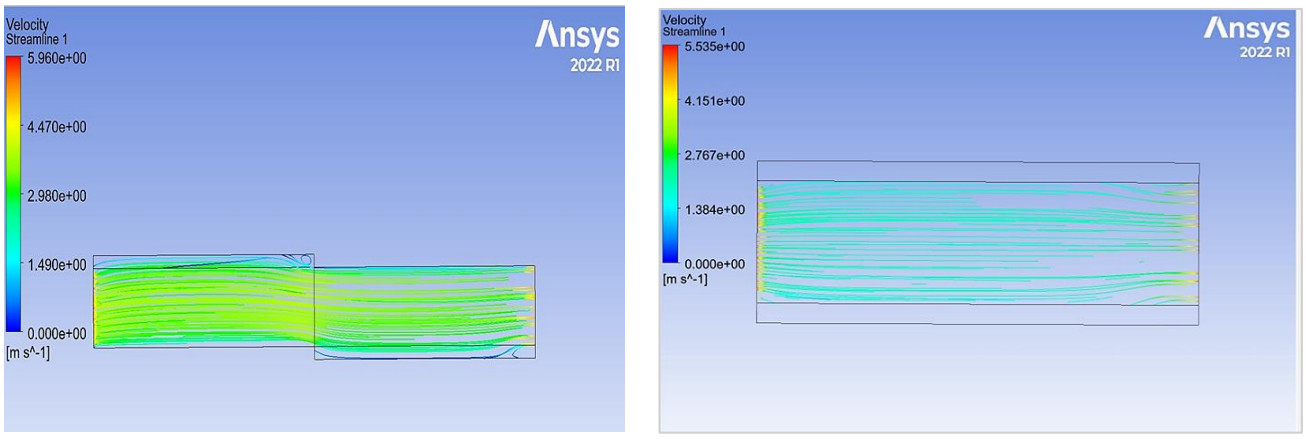

(A) **(B)**

Figure 15: Velocity streamlines of air flow inside heat sinks of cases A) case 1 and B) case 2

The goal of utilizing the previously outlined air properties is to achieve surface condensation by reaching a temperature at the heat exchanger walls corresponding to the dew point. By applying the same conditions to two distinct heatsink cases, which have equivalent surface areas but different air passage dimensions, the results indicate a lower surface temperature in the second case, as shown in Figure 16. In the second case, the dew point temperature was reached at air velocities of 5 m/s and 4 m/s, whereas, in the first case, the dew point temperature at the heatsink wall was not achieved, indicating the absence of condensation. The difference in outcomes can be attributed to the geometric configuration of the air passages in the second case, which facilitates the achievement of lower temperatures due to the thin boundary layer resulting from the narrow air passages. When comparing the two heat exchanger configurations, it was observed that the surface temperature of the first case was significantly higher, displaying a temperature difference of up to 38% compared to the second case. Although a more uniform temperature distribution was observed in the second case, as illustrated in Figure 16, condensation did not occur. This highlights the importance of considering the narrow geometrical spacing of air passages for optimal condensation, ensuring lower temperatures and an increased cooling surface area.

Figure 17 compares the air outlet temperatures from heat sinks and their corresponding velocities. The data indicate that the second scenario achieved the lowest air temperature due to a thin boundary layer adjacent to the fluid flow, facilitating lower temperature achievement. As airflow velocity increases, the temperature difference between the two scenarios narrows, ranging from 1% to 5%. The underlying reason is that higher air speeds enhance airflow, consequently elevating the air outlet temperature. The graph in Figure 17 demonstrates that increased velocity correlates with higher air temperatures. However, a noticeable difference in outlet temperatures between velocities of 4 m/s and 5 m/s is observed. This discrepancy arises from the transitional nature of flow behavior at 5 m/s, indicating that the flow is within a transitional region characterized by an incomplete evolution to fully turbulent flow.

Figure 18 illustrates the correlation between fluid flow velocity and the convection heat transfer coefficient for both cases. The graphical representation shows that the convection coefficient increases with fluid velocity. This phenomenon is attributed to the higher fluid velocity, contributing to an elevated heat transfer rate. Furthermore, the figure demonstrates that the second case exhibits a superior heat transfer coefficient compared to the first case, with the percentage increase in the convective heat transfer coefficient for the second case compared to the first, ranging from 17% to 20%.

This discrepancy is a consequence of the narrower cross-sectional area of the air passage in the second case, which mitigates the impact of the boundary layer and thereby results in an amplified heat transfer through convection. The increased air velocity in the second case also contributes to the higher heat transfer coefficient, as a higher air velocity correlates with an augmented heat transfer rate.

Figure 19 compares cooling efficiency under two airflow scenarios across various airflow velocities. By maintaining the temperature of the aluminum alloy heatsink constant, a significant variation in cooling performance was observed for both scenarios at each velocity. The data in the figure reveal that scenario two outperforms scenario one regarding cooling efficiency, with the difference in performance ranging from 2% to 27%. This superior cooling capability in the second scenario can be attributed to a higher heat transfer coefficient. This enhancement is likely due to the smaller hydraulic diameter of the air channels in the second scenario, facilitating more rapid heat transfer by ensuring more stable airflow through the channels.

Furthermore, Figure 19 demonstrates that the heat transfer rate increases as the airflow velocity increases. This effect is particularly pronounced in scenarios involving narrow passages, which are more effective for heat transfer. This is attributed to the increased convective heat transfer coefficient associated with higher velocities, improving cooling performance.

Figure 20 visually presents the pressure drop between the air inlet and outlet for the two cases examined. The heat transfer amount in the second case is higher than in the first. Case 2 exhibits a significant variance in pressure, primarily attributed to the frictional interactions between the heat sinks and the turbulent airflow. The pressure difference for air entering and exiting in both cases ranges from 15% to 27%.

Furthermore, Figure 20 also shows that the pressure drop escalates with increasing flow velocity due to the turbulent nature of the air and the emergence of vortices near the walls. These vortices impede flow within the boundary layer close to the walls, with a more pronounced effect in the second case due to the smaller cross-sectional area of the air passages in the heat sink.

To evaluate the performance of the heat sink in terms of heat transfer and pressure drop, the ratio of the heat transfer coefficient to pressure drop ($h/\Delta p$) is calculated for each case, as illustrated in Figure 21. The graphical representation indicates an inversely proportional relationship between $h/\Delta p$ and flow velocity. This relationship suggests that an increase in velocity significantly impacts the air pressure differential, with its effect outweighing the heat transfer coefficient due to speed.

Moreover, Figure 21 demonstrates that the first scenario exhibits better thermal performance about pressure drop than the second scenario. The performance difference between the two scenarios ranges from 1% to 3.5%. This difference narrows as velocity increases, attributable to the rise in pressure differential caused by air vortices resulting from turbulent flow. Despite not achieving a temperature lower than the dew point, the first scenario shows lower pressure loss due to the arrangement and larger cross-sectional area of the air passages in the heat sink.

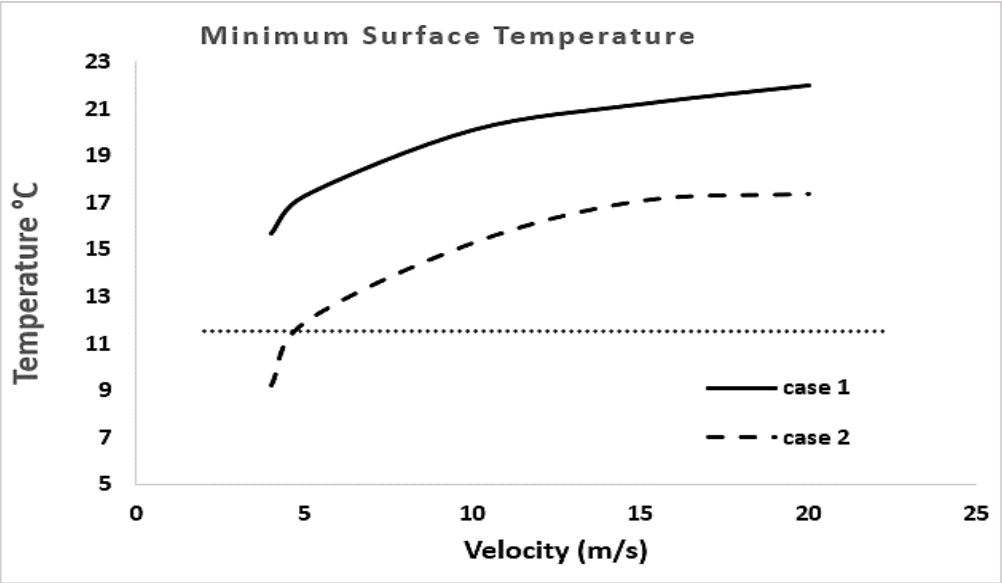

Figure 16: Minimum surface air temperature of two cases with different surface temperatures

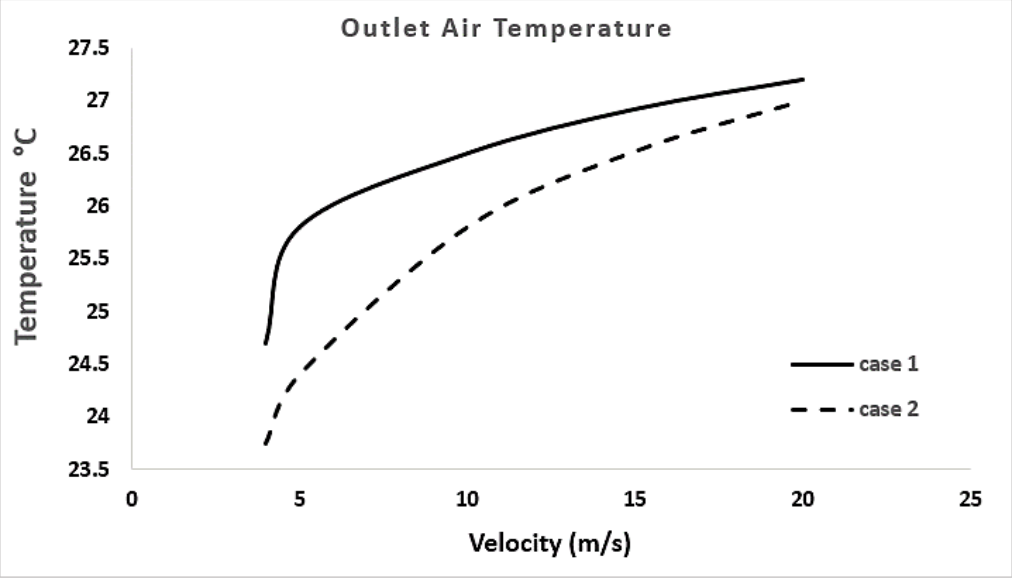

Figure 17: Outlet temperature of two cases with different velocities

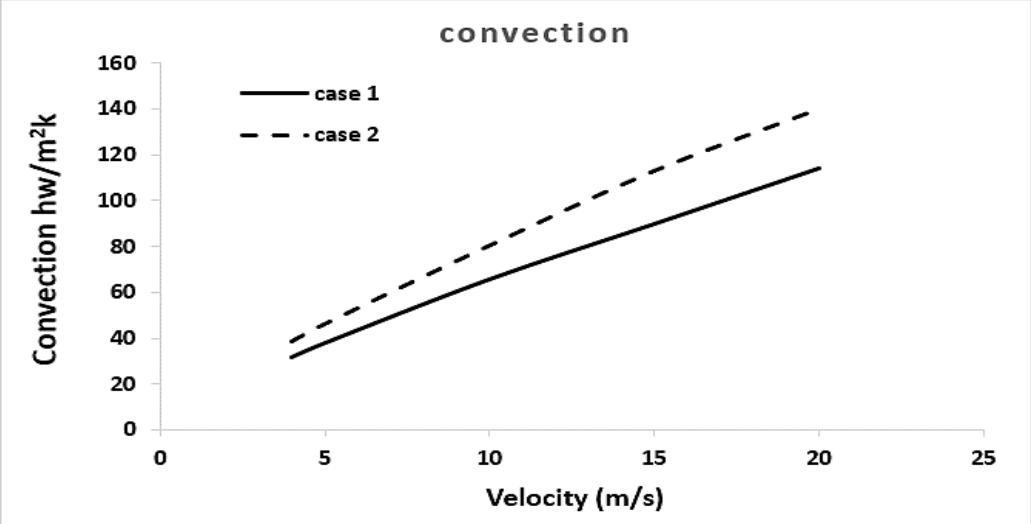

Figure 18: Convection heat transfer coefficient in two cases with different velocities

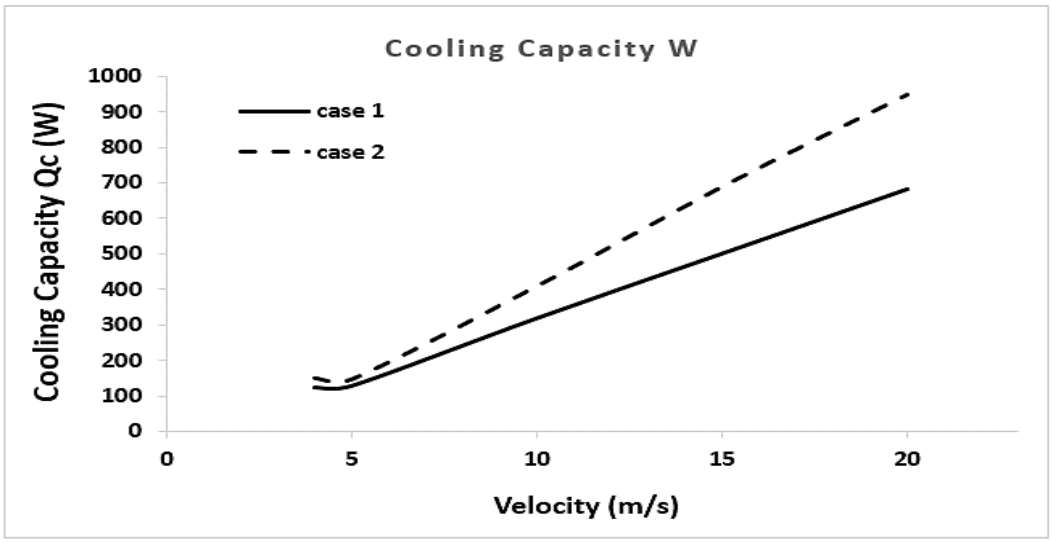

Figure 19: Heat capacity of two cases with different velocities

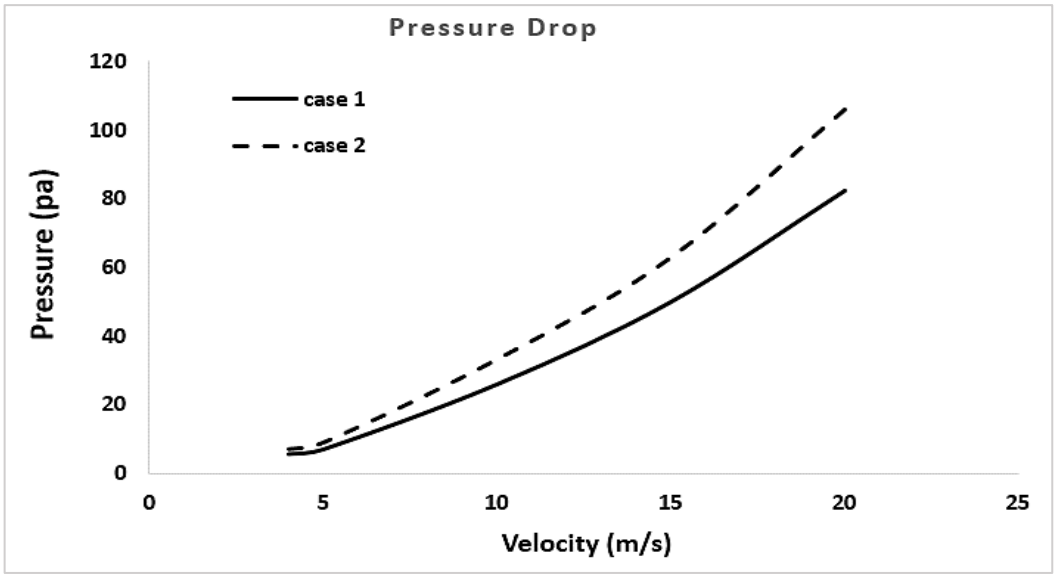

Figure 20: Pressure drop of two cases with different velocities

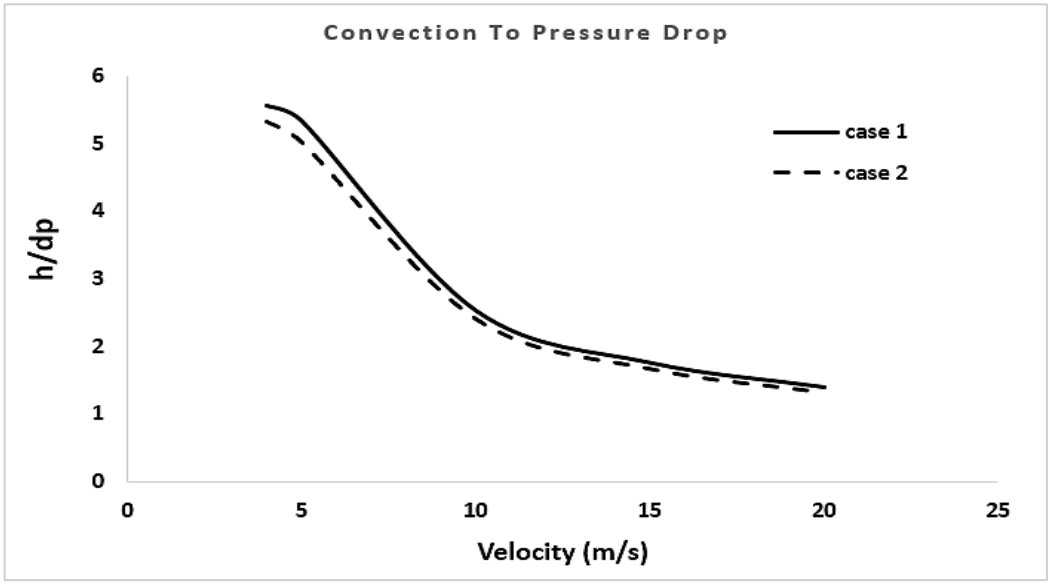

Figure 21: Convection to pressure drop of two cases with different velocities

5. Conclusion

In summary, this study looks into the possibility of reaching the dew point temperature using a heatsink in Basra's climate. We used Fluent 22.1 software for simulations to check the temperature, airflow speed, and air pressure at that area's lowest possible temperature and humidity. The data emanated from the Iraqi Ministry of Agriculture's Meteorological Center in Qurna city on July 1, 2022. It showed the lowest dew point temperature could reach 10.52 ℃ in extreme conditions.

It's crucial to cool the air below its dew point to start making water from the air. Our simulations used a thermoelectric device that heats up on one side and cools down on the other, acting as a heatsink to cool down humid air. This involves guiding the air through heatsinks in a way that encourages condensation. We kept the atmospheric conditions and heatsink surface area the same while changing the airflow speed and how the air moves through the device. Air speeds used from 4 to 20 meters per second. The main findings are:

1) Heatsinks work better at cooling when the air moves slower. Finding the right speed is key to keeping the heatsink air cold enough for water to condense. How the air flows through the heatsink matters a lot for condensation. More surface area and less air can help reach the dew point temperature. The coolest temperature we got was 9.2 $^{\circ}$C with a certain heatsink arrangement and an air speed of 4 meters per second.
2) The cooling capacity of the air increases with the use of the rarefied heat sink as the velocity increases, but at the same time, the surface temperature decreases. The study showed that at a speed of 20 meters per second, the cooling capacity ranges from 600 to 900 watts depending on the airflow condition, and the surface temperatures are approximately 26 to 27 degrees Celsius. Consequently, this reduces the likelihood of condensation occurring.
3) By comparing two configurations of heat exchangers, it was found that the first case exhibited higher surface temperatures, with a temperature difference of up to 38% between the two cases. Meanwhile, the second case demonstrated a higher pressure differential between the inlet and the outlet due to the effect of the boundary layer, with a difference reaching up to 20%.
4) The thermal conductivity for the pressure difference between the two cases was compared to assess the thermal performance. It was revealed that the first case exhibited better thermal conductivity relative to the pressure difference compared to the second case, with a difference of up to 8%.
5) Although the dew point sets a limit, Qurna's weather is good for making water from the air because of its temperature and humidity levels.

Based on the conclusion, we recommend developing a practical case of the condensation process under specific conditions, accounting for changes in airflow patterns. This entails utilizing various heat sink designs to optimize the thermal process for maximum efficiency and speed.

Nomenclature	**Description**	**Units or Symbols**
Ac	Cross section area of a fin	m^2
Af	Fins area	m^2
At	Total area	m^2
Cp	Specific heat	kJ/kg K
COP	Coefficient of Performance	-
D	Diameter	m
Eff	Effectiveness	L/J
f	Fraction factor	-
h	Enthalpy	J/kg
h_{conv}	Convection heat transfer coefficient	W/m^2 K
H	Height of each channel's hole	m
I	Current	A
kf	Thermal conductivity of base air flow	W/m K
ks	Thermal conductivity of base plate material	W/m K
K_m	TEC module thermal conductance	W/K
l	Length	m
lc	Characteristic length	m
N	Number	-
Nu	Nusselt number	-
p	Perimeter	m
P	Power	W
Pr	Prandtl number	-
Q	Transferred heat	W
R	Resistance	K/W
R″	Thermal resistance	m^2 K/W
Rm	TEC module electrical resistance	ohm
Re	Reynolds number	-
Nomenclature	**Description**	**Units or Symbols**
Sm	TEC module Seebeck coefficient	V/K
T	Temperature	K
u	Air velocity	m/s
V	Voltage	V
$\dot{V}$	Volume flow rate of water	L/s
η0	Overall surface efficiency	-
ηf	Efficiency of fin with an adiabatic tip	-
ν	Kinematic viscosity	m^2/s
ΔP	Pressure drop	Pa

ΔT	Temperature difference	K
ρ	Density	kg/m^3
ϕ	Relative humidity	-
a	Ambient	-
c	Cold side	-
equ	Equivalent resistance	-
h	Hot side	-
hyd	Hydraulic	-
LMTD	Log mean temperature difference	-
max	Maximum	-
t, b	Resistance of the un-finned part of the heat sink	-
t, base	Thermal resistance of the base surface	-
t, c	Contact resistance	-
TEC, m	Thermoelectric cooler	-
w	Water	-

Acknowledgment

The authors would like to acknowledge the role of the Iraqi Ministry of Agriculture's Meteorological Center in providing information on the weather conditions in Basra, specifically the city of Qurna.

Author contributions

Conceptualization, A. al-Tajer and W. Alawee; data curation, A. al-Tajer; formal analysis, W. Alawee; investigation, H. Dhahad; methodology, Z. Omara; project administration, H. Dhahad, resources, Z. Omara; software, A. al-Tajer; supervision, H. Dhahad.; validation, A. al-Tajer, W. Alawee and H. Dhahad.; visualization, W. Alawee; writing—original draft preparation, A. al-Tajer; writing—review and editing, A. al-Tajer .All authors have read and agreed to the published version of the manuscript.

Funding

This research received no specific grant from any funding agency in the public, commercial, or not-for-profit sectors.

Data availability statement

The data that support the findings of this study are available on request from the corresponding author.

Conflicts of interest

The authors declare that there is no conflict of interest.

References

[1] P. H. Gleick, The human right to water, Water Policy, 1 (1998) 487–503. https://doi.org/10.1016/S1366-7017(99)00008-2

[2] B. R. Yassein, K. A. Al Asaady, A. A. Kazem, M. T. Chaichan, Environmental Impacts of Salt Tide in Shatt Al-Arab-Basra/Iraq, IOSR J. Environ. Sci., 10 (2016) 35–43.

[3] A. H. Al Obaidy, M. Al-Khateeb, The Challenges of Water Sustainability in Iraq, Eng. Technol. J., 31 (2013) 828–840. https://doi.org/10.30684/etj.31.5a3

[4] A. A. Salehi, M. Ghannadi-Maragheh, M. Torab-Mostaedi, R. Torkaman, M. Asadollahzadeh, A review on the water-energy nexus for drinking water production from humid air, Renew. Sustain. Energy Rev., 120 (2020) 109627. https://doi.org/10.1016/j.rser.2019.109627

[5] Y. Wang, S. H. Danook, H. A. Z. Al-Bonsrulah, D. Veeman, and F. Wang, A Recent and Systematic Review on Water Extraction from the Atmosphere for Arid Zones, Energies, 15 (2022) . https://doi.org/10.3390/en15020421

[6] Y. Tu, R. Wang, Y. Zhang, J. Wang, Progress and Expectation of Atmospheric Water Harvesting, Joule, 2 (2018)1452–1475. https://doi.org/10.1016/j.joule.2018.07.015

[7] Z. Chen et al., Recent progress on sorption/desorption-based atmospheric water harvesting powered by solar energy, Sol. Energy Mater. Sol. Cells, 230 (2021)111233. https://doi.org/10.1016/j.solmat.2021.111233

[8] C. T. Wilson, H. Cha, Y. Zhong, A. C. Li, E. Lin, B. El Fil, Design considerations for next-generation sorbent-based atmospheric water-harvesting devices, device, 1 (2023) 1–14. https://doi.org/10.1016/j.device.2023.100052

[9] S. Srivastava, A. Yadav, Water generation from atmospheric air by using composite desiccant material through fixed focus concentrating solar thermal power, Sol. Energy, 169 (2018) 302–315. https://doi.org/10.1016/j.solener.2018.03.089

[10] V. P. Joshi, V. S. Joshi, H. A. Kothari, M. D. Mahajan, M. B. Chaudhari, K. D. Sant, Experimental Investigations on a Portable Fresh Water Generator Using a Thermoelectric Cooler, Energy Procedia, 109 (2017) 161–166. https://doi.org/10.1016/j.egypro.2017.03.085

[11] M. Eslami, F. Tajeddini, N. Etaati, Thermal analysis and optimization of a system for water harvesting from humid air using thermoelectric coolers, Energy Convers. Manag., 174 (2018) 417–429. https://doi.org/10.1016/j.enconman.2018.08.045

[12] J. S. Solís-Chaves, C. M. Rocha-Osorio, A. L. L. Murari, V. M. Lira, A. J. S. Filho, Extracting potable water from humid air plus electric wind generation: A possible application for a Brazilian prototype, Renew. Energy, 121 (2018) 102–115. https://doi.org/10.1016/j.renene.2017.12.039

[13] M. H. Esfe, S. Esfandeh, D. Toghraie, Numerical simulation of water production from humid air for Khuzestan province: Investigation of the Peltier effect (thermoelectric cooling system) on water production rate, Case Stud. Therm. Eng., 28 (2021) 101473. https://doi.org/10.1016/j.csite.2021.101473

[14] A. M. A. Al-Lami, Z. R. Abbas, A. G. Alshammary, Study of water pollution problem in basra city of Iraq: A case study, Plant Arch., 20 (2020) 2274–2276.

[15] A. A. Mahmood, A. M. Eassa, H. Mohammed, Y. Shubbar, Assessment of ground water quality at Basrah , Iraq by water quality index (WQI), 21 (2013) 2531–2543.

[16] M. Boukhriss, K. Zhani, R. Ghribi, Study of thermophysical properties of a solar desalination system using solar energy, Desalin. Water Treat., 51 (2013) 1290–1295. https://doi.org/10.1080/19443994.2012.714925

[17] M. Eslami, F. Tajeddini, N. Etaati, Thermal analysis and optimization of a system for water harvesting from humid air using thermoelectric coolers, Energy Convers. Manag., 174 (2018) 417–429. https://doi.org/10.1016/j.enconman.2018.08.045

[18] M. G. Lawrence, The relationship between relative humidity and the dewpoint temperature in moist air: A simple conversion and applications, Bull. Am. Meteorol. Soc., 86 (2005) 225–233. https://doi.org/10.1175/BAMS-86-2-225

[19] H. S. Dizaji, S. Jafarmadar, S. Khalilarya, A. Moosavi, An exhaustive experimental study of a novel air-water based thermoelectric cooling unit, Appl. Energy, 181(2016) 357–366. https://doi.org/10.1016/j.apenergy.2016.08.074

[20] Çengel, Y. A., and Boles, M. A., Thermodynamics: An Engineering Approach, 5th ed, McGraw-Hill, 2006.

[21] Cengel, Y. A., Heat Transfer: A Practical Approach. McGraw-Hill Science, 2006.

[22] Holman, J. P., Heat Transfer, 10th ed., United States.: McGraw-Hill Companies, 2010.

[23] A. Zhang, Y. Li, Thermal Conductivity of Aluminum Alloys—A Review, Materials., 16 (2023). https://doi.org/10.3390/ma16082972

[24] White, F. M., Fluid Mechanics, 4th ed., McGraw-Hill, 2001.

[25] Öztürk, E., CFD Analyses Of Heat Sinks For Cpu Cooling With Fluent, M.Sc. thesis, Middle East Technical University, 2004.

[26] Mahmoud, N. S., Investigation Of Heat Transfer Enhancement With Nanofluid And Twisted Tape Inserts In A Circular Tube, University of Technology, 2014.

[27] B. Kanargi, P. S. Lee, C. Yap, A numerical and experimental investigation of heat transfer and fluid flow characteristics of an air-cooled oblique-finned heat sink, Int. J. Heat Mass Transf., 116 (2018) 393–416. https://doi.org/10.1016/j.ijheatmasstransfer.2017.09.013

[28] F. Rondeaux, Ph. Bredy, and J. M. Rey, Thermal conductivity measurements of epoxy systems at low temperature, American Institute of Physics, 197 (2002) 197–203. https://doi.org/10.1063/1.1472543